Dynamic compression of [100] MgF_2 single crystals: Shock-induced polymorphism to highly coordinated structures

I. K. Ocampo [1,*] J. M. Winey [2] Y. Toyoda,[2] and T. S. Duffy[1]
[1]*Department of Geoscience, Princeton University, Princeton, New Jersey 08544, USA*
[2]*Insitute for Shock Physics, Washington State University, Pullman, Washington 99163, USA*

(Received 28 July 2022; accepted 6 October 2022; published 25 October 2022)

AX_2-type compounds exhibit a rich and complex series of phase transitions under compression. The high-pressure polymorphism of rutile-type AX_2 difluorides can be characterized by a typical sequence from rutile type → $CaCl_2$ type → HP-PdF_2 type → cotunnite type. Relative to dioxides, the reduced valence and ionic radius of the F^- anion in rutile-type MgF_2 (sellaite) results in lowered transition pressures, making it a useful analog for SiO_2 and other dioxides. In this work, MgF_2 single crystals were shock-compressed along the [100] direction to 24 to 120 GPa using plate impact techniques, and wave profiles were measured using laser interferometry. At low stresses (24 to 44 GPa), we observe features consistent with an elastic–inelastic response, followed by a phase transformation. Peak stress-density states in this stress range are consistent with those expected for the modified fluorite-type (HP-PdF_2) phase or a related structure. At higher stresses (69 to 91 GPa), we observe a two-wave structure with peak stress-density states consistent with transformation to a denser and likely more highly coordinated phase such as the cotunnite-type structure. At 120 GPa, only a single wave structure is observed, indicating that the wave profile features observed at lower stresses are overdriven.

DOI: 10.1103/PhysRevB.106.144108

I. INTRODUCTION

Magnesium difluoride (MgF_2) is an archetypal, simple ionic solid and, as such, has been extensively studied using theory and experiments to determine its pressure-induced polymorphism [1–6]. Exhibiting wide optical transmission (UV to infrared) and a low refractive index, MgF_2 is commonly used for optical windows and antireflective coatings [7]. MgF_2 occurs naturally as the mineral sellaite with the rutile-type ($P4_2/mnm$) structure at ambient conditions. Under quasi-hydrostatic loading at room temperature, MgF_2 has been observed to transform to a $CaCl_2$-type structure ($Pnmn$) at 9 GPa, a modified fluorite-type structure [high-pressure (HP)-PdF_2-type, $Pa\bar{3}$] at 14 GPa, and an α-$PbCl_2$ or cotunnite-type structure ($Pnma$) above 35 GPa, resulting in an increase in cation coordination from six (rutile type) to nine (cotunnite type) [1,2,8]. An α-PbO_2-type (distorted rutile) structure has been reported upon pressure release, and at high temperatures (600 to 750 °C) has been reported to exhibit a narrow region of stability at ∼13 GPa [2].

In previous literature, the so-called modified fluorite-type structure with the $Pa\bar{3}$ space group has been described by a variety of names (i.e., pyrite, distorted fluorite, HP-PdF_2), especially in the context of the high-pressure cubic polymorph of SiO_2 [3,9,10]. The pyrite (FeS_2) and HP-PdF_2 structures adopt an fcc arrangement of cations, but exhibit deviations in the anion lattice position from the ideal fluorite structure. The pyrite-type structure is characterized by anion–anion bonding, which is distinctly absent in AX_2-type oxides and difluorides such as SiO_2 and MnF_2 [11,12]. As a result, we refer to the modified fluorite-type cubic structure as the HP-PdF_2-type hereafter.

This observed family of phase transformations is common among AX_2 compounds, making MgF_2 isostructural with geophysically relevant materials such as stishovite, a high-pressure polymorph of SiO_2, and rutile, TiO_2 [9,13]. Both stishovite and rutile (along with its high-pressure polymorphs riesite, akaogiite, and srilankite) are products recovered at meteorite impact sites [14]. Sellaite has also been observed as inclusions in deep mantle-derived diamonds [15]. To understand more fully the shock, release, and recovery of mineral assemblages used to characterize the shock conditions during meteorite impacts, knowledge of the response of AX_2-type solids to the pressures, temperatures, and strain rates of meteorite impacts is required.

Relative to dioxides, the reduced valence and ionic radius of the F^- anion in difluorides results in elastic weakening, lower melting temperature, and lower phase transition pressures, making them useful analogs for dioxides under the extreme pressure–temperature conditions associated with exoplanetary interiors [1,16]. For example, $NaMgF_3$ and its breakdown products, NaF and MgF_2, have recently been proposed as an analog system for the dissociation of $MgSiO_3$, Mg_2SiO_4, and $MgSi_2O_5$ to $MgO + SiO_2$ [8,16,17]. As silica is predicted to undergo a HP-PdF_2-type–to–cotunnite-type phase transformation at pressures greater than 600 GPa [10,16,18], far exceeding those accessible using standard static loading techniques, low-pressure analogs such as MgF_2 can be used to study these transformation pathways at more readily accessible laboratory conditions.

Limited data are available for the response of MgF_2 to dynamic loading. Bugaeva *et al.* [19] reported explosively

*iocampo@princeton.edu

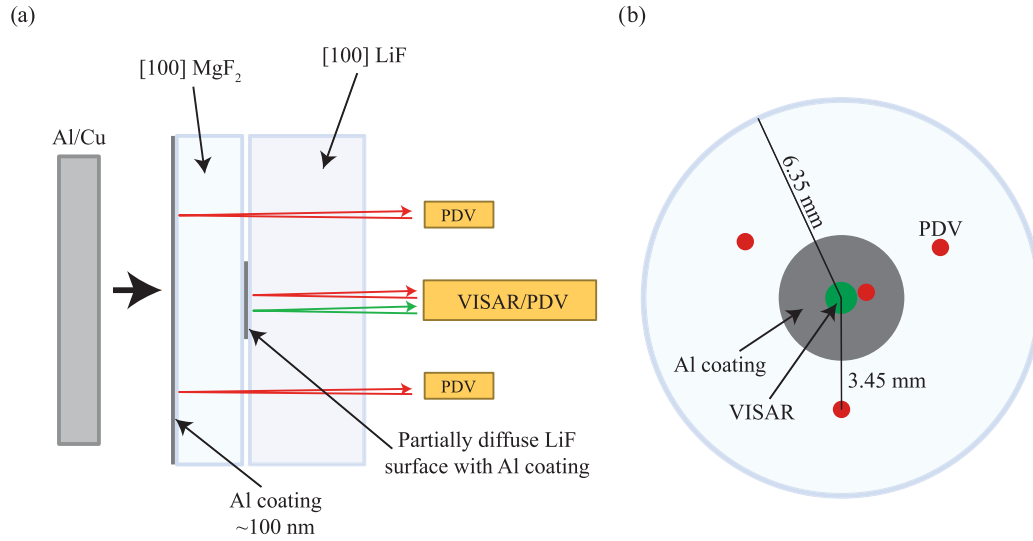

FIG. 1. Schematic illustration of the experimental configuration used in the plate impact experiments. (a) Side view and (b) back view of sample assembly and probe configuration.

driven plate impact experiments on polycrystalline MgF_2 in which shock-wave arrivals were measured using an electrical shorting pin method. Although shorting pin methods have been used extensively in the past to measure single-wave Hugoniot states, they do not provide wave profile information. In particular, multiwave structures—such as those arising due to elastic–inelastic response and/or phase transformations—cannot be properly characterized using this method. Previous continuum-level measurements of the shock response of fluorite-structured difluorides (CaF_2, PbF_2, BaF_2) show volume changes suggestive of phase transformations [20–24]. In addition, a recent *in situ* x-ray diffraction study on dynamically compressed porous CaF_2 reported observation of the fluorite-to-cotunnite transformation on nanosecond timescales [22]. Therefore, wave profile measurements are needed to examine phase stability in shock-compressed MgF_2. Here, we present the results of plate impact experiments to measure wave profiles in MgF_2 shock compressed along the [100] direction to understand more fully the response of this fundamental material to dynamic loading.

II. EXPERIMENTAL METHODS

Magnesium difluoride [100] single crystals were obtained from Optocity (Raleigh, NC). This crystal orientation was chosen due to the low elastic stiffness relative to that along the symmetry axis ($c_{11} = 143.5$ GPa, $c_{33} = 208.8$ GPa) [4]. The samples were double-side–polished to a mirror finish with a high degree of flatness and parallelism ($<2-\mu$m variation over the surface). The orientation of each crystal was measured using Laue back-reflection imaging and were confirmed to be within 1 ° of the [100] axis. The ambient density (ρ_0) was determined to be 3.179(5) g/cm^3 using the Archimedean method, consistent with values from the literature [1,4]. Ambient longitudinal (C_L) and shear (C_{s1}, C_{s2}) sound speeds were measured to be 6.67(2), 5.50(1), and 4.23(1) km/s, respectively, using the pulse-echo method with 20-MHz transducers. Numbers shown in parentheses are one-standard deviation uncertainties in the last digit of the stated value. These measured values are consistent with those calculated from elastic constants measured at ambient conditions (6.72, 5.52, and 4.26 km/s) [25].

A schematic illustration of the target configuration is shown in Fig. 1. A ∼100-nm aluminum mirror was vapor-deposited on the impact surface of the MgF_2 single crystals. The MgF_2 samples were bonded to [100]-oriented LiF windows. A thin, partially diffuse aluminum mirror was vapor-deposited onto the center of the LiF window prior to bonding. Epoxy bonds for all targets were measured to be <1 μm thick. The sample assemblies were impacted with either an oxygen-free electronic (OFE) C101 copper or 1050 aluminum impactor mounted in a polymethylpentene (TPX) projectile and launched by either a powder gun or a two-stage gas gun at the Institute for Shock Physics at Washington State University. Projectile velocities were measured using a velocity optical beam block system with typical precisions of $< 0.3\%$. Three noncolinear photon Doppler velocimetry (PDV) probes (1550 nm) [26] were radially positioned at 120 ° intervals and focused onto the sample front surface to record the impact time and projectile tilt, as well as transparency of the sample throughout the duration of the experiment. Particle velocity histories at the sample–LiF interface were recorded using a combination Velocity Interferometer System for Any Reflector (VISAR; 532 nm) [27] and PDV probe. Two VISAR channels with differing velocity sensitivities (0.423 km/s/fringe and 1.036 km/s/fringe) were used to unambiguously resolve any discontinuities in the particle velocity history. Wave profiles measured using PDV showed good agreement with those from VISAR. Sample dimensions were chosen to maintain the uniaxial strain condition at the position of the wave profile measurement until the end of the experiment.

III. RESULTS AND DISCUSSION

Eight plate impact experiments were performed. The experimental parameters for each shot are shown in Table I. Wave profiles were measured at the sample–LiF interface and

TABLE I. Summary of experimental parameters.

Experiment	MgF_2 thickness (mm)[a]	Impactor	Impactor thickness (mm)[a]	Projectile velocity (km/s)[b]
1 (21-606)	2.074	1050 Al	1.333	2.479
2 (21-608)	2.041	OFE Cu	1.372	1.995
3 (21-607)	2.076	OFE Cu	1.409	2.400
4 (20-2SH60)	2.078	1050 Al	1.426	4.010
5 (21-2SH06)	2.041	1050 Al	1.375	4.967
6 (20-2SH57)	2.077	1050 Al	1.393	5.582
7 (20-2SH61)	2.077	1050 Al	1.411	6.708
8 (21-2SH07)	2.039	OFE Cu	0.971	5.845

[a]Uncertainties in thickness measurements are 1 to 2 μm.
[b]Uncertainties in projectile velocities are <0.3%.

were corrected for the changes in the refractive index of LiF due to shock compression [28]. Figure 2 shows the results from the VISAR measurements; the PDV results are similar. At lower stresses, the measured profiles show three distinct waves, whereas two waves are observed at higher stresses. Only a single wave is observed at the highest stress. To analyze the measured wave profiles quantitatively, the following procedures were used.

Lagrangian shock wave velocities for the different waves in the profiles were determined using the measured thickness of each MgF_2 sample, and the transit times as measured using the PDV probe array. *In situ* particle velocities in the MgF_2 sample were determined from the measured MgF_2–LiF interface velocities using an impedance-matching analysis [29,30], described later, that incorporated the published LiF Hugoniot curve [28]. Because MgF_2 and LiF have similar shock impedances (Supplemental Material Fig. S1 [31]), differences between the measured interface velocities and the in-material MgF_2 velocities are small. For profiles exhibiting a multiwave

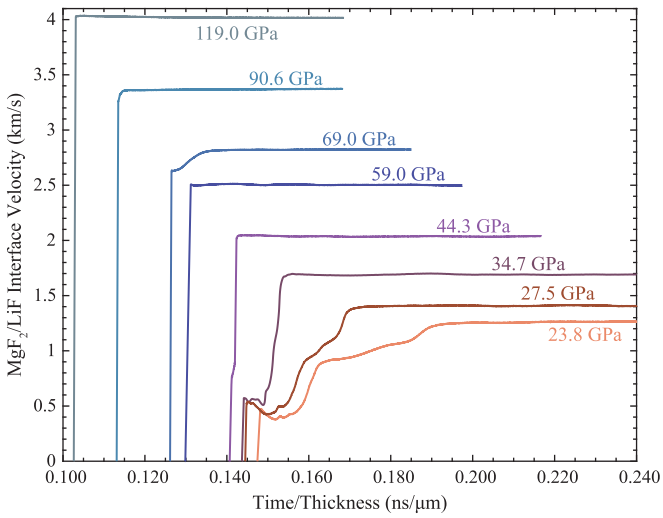

FIG. 2. Particle velocity histories at the MgF_2–LiF interface, corrected for the refractive index change in LiF due to shock compression [28]. Velocity profiles shown are obtained from the VISAR channel having higher velocity resolution (0.423 km/s/fringe). Time is normalized to the sample thickness, so that wave arrivals equate to the reciprocal of the Lagrangian shock velocity. The peak stresses shown are from Table II.

structure, we approximated the particle velocity history using a sequence of step functions (Supplemental Material Fig. S2 [31]), where the jump in particle velocity at each step is positioned at the approximate midpoint of each shock-wave arrival. Longitudinal stress (σ_x)—chosen to be positive in compression—and density (ρ) at each step were calculated using the Rankine–Hugoniot jump conditions for the conservation of mass and momentum:

First shock:

$$U_{S,1} = \frac{h}{t_1}, \tag{1}$$

$$\rho_0 U_{S,1} = \rho_1 (U_{S,1} - u_1), \tag{2}$$

and

$$\sigma_{x,1} = \rho_0 U_{S,1} u_1. \tag{3}$$

Ensuing shocks:

$$U_{S,i} = \frac{\rho_0}{\rho_{i-1}} \left(\frac{h}{t_i} \right), \tag{4}$$

$$\rho_{i-1} U_{S,i} = \rho_i [U_{S,i} - (u_i - u_{i-1})], \tag{5}$$

and

$$\sigma_{x,i} - \sigma_{x,i-1} = \rho_{i-1} U_{S,i} (u_i - u_{i-1}). \tag{6}$$

In Eqs. (1)–(6), ρ_0 is the initial density, h is the initial sample thickness, t is the shock-wave arrival time, and U_S is the Eulerian shock velocity, which accounts for the sample thickness change due to compression from preceding shock waves. The particle velocities (u) are expressed in the laboratory reference frame, and the index (i) is used to denote the arrival times and continuum variables associated with each successive shock in the multistep analysis. A graphical schematic of this multistep impedance-match analysis is shown in Supplemental Material Fig. S3 for the case of a two-step wave [31]. Uncertainties in sample metrology, projectile velocity, transit time, and the measured interface particle velocities are propagated using a Monte Carlo multistep (MCMS) impedance-match algorithm with 1 000 000 simulations per experiment. Table II summarizes these results.

As shown in in Fig. 2, for wave profiles with peak stresses ranging from 24 to 44 GPa, we observe an elastic–inelastic

TABLE II. Results from shock-wave profile measurements on [100]-oriented MgF_2 single crystals. The particle velocity (u), longitudinal stress (σ_x), and density (ρ) states are determined using the MCMS impedance match algorithm. Eulerian shock velocities (U_S) are determined using PDV transit time measurements and the density compression (ρ_0/ρ) ratio. Numbers shown in parentheses are the one-standard deviation uncertainty in the last digit(s) in the reported value as determined by the MCMS analysis.

	Elastic wave				Inelastic wave				Final wave			
Experiment	u (km/s)	U_S (km/s)	σ_x (GPa)	ρ (g/cm^3)	u (km/s)	U_S (km/s)	σ_x (GPa)	ρ (g/cm^3)	u (km/s)	U_S (km/s)	σ_x (GPa)	ρ (g/cm^3)
1 (21-606)	0.404(2)	6.77(2)	8.69(5)	3.381(2)	0.839(10)	5.89(2)	17.4(2)	3.651(9)	1.214(9)	4.70(4)	23.8(2)	3.968(11)
2 (21-608)	0.461(3)	6.92(2)	10.1(1)	3.406(2)	0.858(8)	5.96(2)	18.2(2)	3.649(8)	1.351(10)	5.20(2)	27.5(2)	4.031(11)
3 (21-607)	0.524(3)	6.95(2)	11.6(1)	3.438(2)	–	–	–	–	1.630(12)	6.09(2)	34.7(3)	4.200(13)
4 (20-2SH60)	0.667(4)	7.10(3)	15.1(1)	3.509(3)	–	–	–	–	1.975(15)	6.37(2)	44.3(3)	4.415(15)
5 (21-2SH06)[a]	–	–	–	–	–	–	–	–	2.420(19)	7.66(4)	59.0(5)	4.647(23)
6 (20-2SH57)[a]	–	–	–	–	2.523(20)	7.92(3)	63.5(5)	4.666(21)	2.747(22)	5.20(3)	69.0(5)	4.876(26)
7 (20-2SH61)[a]	–	–	–	–	3.106(25)	8.83(4)	87.2(7)	4.904(27)	3.229(26)	5.68(4)	90.6(7)	5.013(29)
8 (21-2SH07)[a]	–	–	–	–	–	–	–	–	3.851(32)	9.72(5)	119.0(10)	5.265(38)

[a]Elastic wave was overdriven in experiments 5 through 8.

response, followed by structure indicating a phase transformation. The speed of the first wave (corresponding to the reciprocal of the arrival time in Fig. 2) in the four experiments in this stress range is consistent with elastically compressed rutile-type MgF_2. The elastic-wave amplitude is observed to range from 8.69 to 15.1 GPa, depending on the peak shock stress. After arrival of the elastic wave, the particle velocity decreases significantly prior to the arrival of the intermediate or inelastic wave, indicating considerable stress relaxation. Subsequent to the inelastic wave, the arrival of a third wave suggests the onset of a phase transformation; at the lowest stresses (24 to 27 GPa), the third wave involves significant ramping behavior (Fig. 2). At 44 GPa, the elastic precursor is nearly overdriven, and at 59 GPa, only a single wave is observed. At 69 GPa, a two-wave structure is again observed. The arrival of the first wave at this stress corresponds to a sharp rise, followed by a second wave that exhibits a ramp-like, time-dependent structure (Fig. 2). The gradual increase in particle velocity associated with the second wave is observed up to 91 GPa (Supplemental Material Fig. S4 [31]). At 120 GPa, only a single flat-top wave is observed, indicating that the wave profile features observed at lower stress have been overdriven.

The σ_x-V states ($V = 1/\rho$) for the elastic, inelastic, and final shock states from this study are shown in comparison to previous shock and static experiments in Fig. 3. We observe two distinct regions exhibiting multiwave structured wave profiles. In the lower stress region (24 to 44 GPa), the first wave is consistent with elastically compressed rutile-type MgF_2 and shows good agreement with results reported for shocked polycrystalline MgF_2 by Bugaeva *et al.* [19] and reasonable agreement with results obtained under static loading [1,2]. The inelastic (or intermediate) wave in this lower stress region is nearly overdriven at 35 GPa and is entirely overdriven at 44 GPa. The peak σ_x-V states for all four experiments in the low-stress region are largely consistent with the HP-PdF_2-type structure reported in both room temperature and laser-heated diamond anvil cell (DAC) experiments [1,2,8]. The peak σ_x-V states presented here differ somewhat from those reported previously for polycrystalline MgF_2 [19]. As noted earlier, the previous Hugoniot measurements used techniques that are insensitive to multiwave features, likely resulting in errors in the reported Hugoniot states. Our wave profile measurements provide a more complete characterization of the material response under dynamic loading and yield a more accurate reporting of the final σ_x-V states in the sample.

From 44 to 59 GPa, the final Hugoniot state becomes clearly denser than the room-temperature static data for the

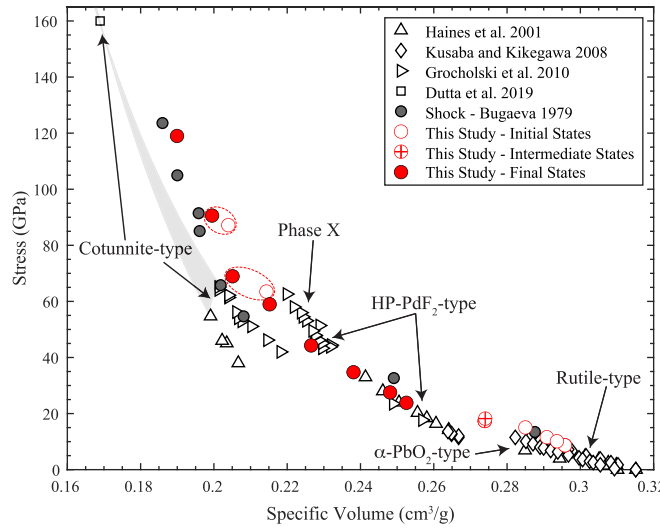

FIG. 3. Longitudinal stress-specific volume states determined in this study are shown as unfilled (initial shocked states), unfilled with crosshairs (intermediate shocked states), and filled (final shocked states) red circles. The dashed red ellipses connect the initial and final states for experiments 4 and 6. For the present data, the error bars are smaller than the size of the marker. Previous shock-wave results [19] are shown as filled black circles (uncertainties were not reported). Static compression results are shown as unfilled black markers [1,2,8]. As the static compression experiments are performed under quasi-hydrostatic conditions, they correspond to pressure states. The gray shaded region illustrates a range of possible pressure–volume states for quasi-statically compressed cotunnite-type MgF_2 based on existing data.

HP-PdF_2-type structure, suggesting that MgF_2 undergoes a transformation to a denser phase or mixed-phase assemblage. Further evidence for a phase change is observed at higher stresses (69 to 91 GPa), where the two-wave profiles are indicative of a large-volume-collapse ($\sim 4\%$) phase change, as shown in Fig. 3. Candidate crystal structures for this higher density phase include the cotunnite-type structure observed under static loading above 35 GPa at room temperature and the proposed SrI_2 or baddeleyite-type "phase X" observed in laser-heated DAC experiments between the stability fields of the HP-PdF_2 and cotunnite-type structures at temperatures above 1500 K [1,8,17]. Grocholski *et al.* [8] report that no orthorhombic solutions satisfy the expected lattice parameter ratios for the SrI_2-type structure, indicating that the monoclinic baddeleyite-type structure (cation coordination of seven) may be the likely structure of phase X. The calculated peak densities from 59 to 120 GPa are greater than those reported for the baddeleyite-type phase X, therefore precluding phase X as the high-stress phase. While there is disagreement as to the density of the cotunnite structure from static compression at 38 to 64 GPa (see Fig. 3), our data are generally consistent with the pressure–volume trend of the cotunnite-type structure [1,8,17], considering the higher temperatures of shock experiments compared to static compression experiments. A single datum for MgF_2 cotunnite reported by Dutta *et al.* [17] at 160 GPa from decomposition of $NaMgF_3$ demonstrates the stability of the cotunnite structure at higher stresses and provides additional constraints on the compression curve. Although the HP-PdF_2–to–cotunnite-type phase transition requires a large cation coordination increase from six to nine, and as a result may be kinetically inhibited, this reconstructive transformation has previously been observed to take place using *in situ* x-ray diffraction in dynamically compressed CaF_2 under the approximately hundred-nanosecond timescales of plate impact shock compression [22]. Furthermore, when compared to the density–compression behavior of CaF_2 under shock loading (Supplemental Material Fig. S5 [31]), our data show remarkable similarity, further bolstering the idea that the cotunnite-type structure may also be synthesized in MgF_2 under shock loading. It is worth noting that the rounding observed near the peak of the 91-GPa wave profile (Supplemental Material Fig. S4 [31]) is similar to that reported previously for shock-compressed silver [32], where the feature was associated with the melting transition. To determine whether the observed wave profile features at 91 GPa and the associated densification are indicative of a crystalline solid–solid phase transition, melting, or amorphization, *in situ* x-ray diffraction measurements on shock-compressed MgF_2 are required. In comparison to the previous shock measurements, our peak σ_x-ρ states are less compressible than those reported in Bugaeva *et al.* [19] from 60 to 120 GPa, but the divergence between these two datasets decreases with increasing stress. As the accuracy of the experimental and analytical methods reported in Bugaeva *et al.* [19] is expected to increase at higher stresses, where the effects of multiwave structures are reduced, the high-stress convergence of our results and theirs may perhaps imply formation of the same phase for both polycrystalline and single-crystal MgF_2 at high shock stresses.

Lastly, our experimental configuration allowed us to monitor the transparency of [100] MgF_2 using the PDV probe array discussed in Sec. II. We find that MgF_2 remains transparent at the 1550-nm wavelength at stresses up to 120 GPa (Supplemental Material Fig. S6 [31]), which is a surprising finding considering the likely solid–solid phase transformations encountered at lower stresses. Experiments at stresses above 120 GPa are needed to determine the stress limit for transparency in shock-compressed MgF_2. Fluorides have long been used as transparent tamper and optical window materials in laser interferometry diagnostics during dynamic compression experiments [28,33–35]. However, the birefringent optical response evident in Supplemental Material Fig. S6 [31] likely limits the usefulness of [100] MgF_2 as an optical window for interferometry at high stresses.

IV. CONCLUSION

Plate impact experiments were conducted on [100] MgF_2 single crystals, reaching peak stresses of 24 to 120 GPa. Wave profiles were measured using laser interferometry, providing highly accurate stress-density states for dynamically compressed single-crystal MgF_2. We find that between 24 and 44 GPa, a multiwave structure is observed, suggesting transformation to a high-pressure phase; the peak stress-density states are most consistent with the HP-PdF_2-type structure (modified fluorite). Above 69 GPa, we observe a time-dependent two-wave structure, with peak stress-density states most consistent with the cotunnite-type structure. To identify these high-stress phases definitively, *in situ* x-ray diffraction on shock-compressed MgF_2 is required. We also find that, despite evidence for multiple phase transitions, [100] MgF_2 remains transparent under shock compression to 120 GPa.

ACKNOWLEDGMENTS

We thank N. Arganbright and K. Zimmerman for their invaluable assistance with the plate impact experiments. We thank Y. M. Gupta for helpful discussions. This work was supported by the U.S. Department of Energy, National Nuclear Security Administration under Cooperative Agreement DE-NA0003957.

[1] J. Haines, J. M. Léger, F. Gorelli, D. D. Klug, J. S. Tse, and Z. Q. Li, X-ray diffraction and theoretical studies of the high-pressure structures and phase transitions in magnesium fluoride, Phys. Rev. B **64**, 134110 (2001).

[2] K. Kusaba and T. Kikegawa, Stable phase with the α-PbO_2-type structure in MgF_2 under high pressure and high temperature, Solid State Commun. **148**, 440 (2008).

[3] J. R. Nelson, R. J. Needs, and C. J. Pickard, High-pressure phases of group-II difluorides: Polymorphism and superionicity, Phys. Rev. B **95**, 054118 (2017).

[4] I. S. Zouboulis, F. Jiang, J. Wang, and T. S. Duffy, Single-crystal elastic constants of magnesium difluoride (MgF_2) to 7.4GPa, J. Phys. Chem. Solids **75**, 136 (2014).

[5] K. Nishidate, M. Baba, T. Sato, and K. Nishikawa, Molecular-dynamics studies on the shock-induced phase transition of a MgF_2 crystal, Phys. Rev. B **52**, 3170 (1995).

[6] V. Kanchana, G. Vaitheeswaran, and M. Rajagopalan, High-pressure structural phase transitions in magnesium fluoride studied by electronic structure calculations, J. Alloys Compd. **352**, 60 (2003).

[7] M. Motamedi, F. Crisostomo, Y. Yao, S. S. Mofarah, W.- F. Chen, P. Koshy, and R. A. Taylor, Single-layer, anti-reflective thin films of porous MgF_2 for solar thermal applications, J. Phys. D Appl. Phys. **52**, 315501 (2019).

[8] B. Grocholski, S.-H. Shim, and V. B. Prakapenka, Stability of the $MgSiO_3$ analog $NaMgF_3$ and its implication for mantle structure in super-earths, Geophys. Res. Lett. **37**, L14204 (2010).

[9] S. Wu, K. Umemoto, M. Ji, C.- Z. Wang, K.- M. Ho, and R. M. Wentzcovitch, Identification of post-pyrite phase transitions in SiO_2 by a genetic algorithm, Phys. Rev. B **83**, 184102 (2011).

[10] T. Tsuchiya and J. Tsuchiya, Prediction of a hexagonal SiO_2 phase affecting stabilities of $MgSiO_3$ and $CaSiO_3$ at multi-megabar pressures, Proc. Natl. Acad. Sci. USA **108**, 1252 (2011).

[11] E. Stavrou, Y. Yao, A. F. Goncharov, Z. Konôpková, and C. Raptis, High-pressure structural study of MnF_2, Phys. Rev. B **93**, 054101 (2016).

[12] Y. Kuwayama, K. Hirose, N. Sata, and Y. Ohishi, Pressure-induced structural evolution of pyrite-type SiO_2, Phys Chem Minerals **38**, 591 (2011).

[13] O. Tschauner, High-pressure minerals, Am. Mineral. **104**, 1701 (2019).

[14] M. Miyahara, N. Tomioka, and L. Bindi, Natural and experimental high-pressure, shock-produced terrestrial and extraterrestrial materials, Prog. Earth Planet Sci. **8**, 59 (2021).

[15] O. Tschauner *et al.*, Ice-VII inclusions in diamonds: Evidence for aqueous fluid in Earth's deep mantle, Science **359**, 1136 (2018).

[16] K. Umemoto, R. M. Wentzcovitch, D. J. Weidner, and J. B. Parise, $NaMgF_3$: A low-pressure analog of $MgSiO_3$, Geophys. Res. Lett. **33**, L15304 (2006).

[17] R. Dutta, E. Greenberg, V. B. Prakapenka, and T. S. Duffy, Phase transitions beyond post-perovskite in $NaMgF_3$ to 160 GPa, Proc. Natl. Acad. Sci. USA **116**, 19324 (2019).

[18] A. R. Oganov, M. J. Gillan, and G. D. Price, Structural stability of silica at high pressures and temperatures, Phys. Rev. B **71**, 064104 (2005).

[19] V. A. Bugaeva, M. A. Podurets, G. V. Simakov, G. S. Telegin, and R. F. Trunin, Dynamic compressibility and state equations of the minerals of rutile structure, Izvestiya Akademii Nauk SSSR Fizika Zemli **1**, 28 (1979).

[20] R. F. Trunin, L. F. Gudarenko, M. V. Zhernokletov, and G. V. Simakov, *Experimental Data on Shock Compressibility and Adiabatic Expansion of Condensed Substances, RFNC-VNIIEF* (RFNC, Sarov, 2001).

[21] L. V. Al'tshuler, M. A. Podurets, G. V. Simakov, and R. F. Trunin, High-density forms of fluorite and rutile, Fiz. Tverd. Tela **15**, 1436 (1973).

[22] P. Kalita, P. Specht, S. Root, N. Sinclair, A. Schuman, M. White, A. L. Cornelius, J. Smith, and S. Sinogeikin, Direct Observations of a Dynamically Driven Phase Transition with in Situ x-ray Diffraction in a Simple Ionic Crystal, Phys. Rev. Lett. **119**, 255701 (2017).

[23] X. Liu *et al.*, Shock-induced polymorphic transitions of PbF_2 up to 1 TPa and their implications for the universal behavior of shocked AX_2 compounds, Phys. Rev. B **103**, 094106 (2021).

[24] S. P. Marsh, *LASL Shock Hugoniot Data* (University of California Press, Berkeley, 1980).

[25] S. Haussühl, Elastisches und thermoelastisches verhalten von MgF_2 und MnF_2, Phys. Status Solidi B **28**, 127 (1968).

[26] O. T. Strand, D. R. Goosman, C. Martinez, T. L. Whitworth, and W. W. Kuhlow, Compact system for high-speed velocimetry using heterodyne techniques, Rev. Sci. Instrum. **77**, 083108 (2006).

[27] L. M. Barker and R. E. Hollenbach, Laser interferometer for measuring high velocities of any reflecting surface, J. Appl. Phys. **43**, 4669 (1972).

[28] P. A. Rigg, M. D. Knudson, R. J. Scharff, and R. S. Hixson, Determining the refractive index of shocked [100] lithium fluoride to the limit of transmissibility, J. Appl. Phys. **116**, 033515 (2014).

[29] J. W. Forbes, *Shock Wave Compression of Condensed Matter: A Primer* (Springer, Berlin, 2012).

[30] S. J. Turneaure, J. M. Winey, and Y. M. Gupta, Response of a Zr-based bulk amorphous alloy to shock wave compression, J. Appl. Phys. **100**, 063522 (2006).

[31] See Supplemental Material at http://link.aps.org/supplemental/10.1103/PhysRevB.106.144108 for additional figures relevant to the discussion, which includes Ref. [36].

[32] M. K. Wallace, J. M. Winey, and Y. M. Gupta, Shock compression of silver to 300 GPa: Wave profile measurements and melting transition, Phys. Rev. B **104**, 014101 (2021).

[33] Y. M. Gupta, *Shock Waves in Condensed Matter* (Springer US, Boston, 1986).

[34] L. E. Kirsch, S. J. Ali, D. E. Fratanduono, R. G. Kraus, D. G. Braun, A. Fernandez-Pañella, R. F. Smith, J. M. McNaney, and J. H. Eggert, Refractive index of lithium fluoride to 900 gigapascal and implications for dynamic equation of state measurements, J. Appl. Phys. **125**, 175901 (2019).

[35] D. E. Fratanduono, T. R. Boehly, P. M. Celliers, M. A. Barrios, J. H. Eggert, R. F. Smith, D. G. Hicks, G. W. Collins, and D. D. Meyerhofer, The direct measurement of ablation pressure driven by 351-nm laser radiation, J. Appl. Phys. **110**, 073110 (2011).

[36] S. Root, M. Desjarlais, R. Lemke, P. Kalita, and S. Alexander, Sandia National Laboratory Report No. SAND2018-0182C (Sandia National Laboratories, Albuquerque, 2018).